Energy Advances

ROYAL SOCIETY OF CHEMISTRY

PAPER

View Article Online
View Journal | View Issue

Check for updates

Cite this: *Energy Adv.*, 2024, 3, 648

Prussian blue-derived FeN_x/Fe-based N-doped carbon nanotube catalysts with high ORR electrochemical performance†

Zhenlu Zhao, ‡*[ab] Qidi Lu‡[a] and Xin Wang[a]

Received 19th December 2023,
Accepted 11th February 2024

DOI: 10.1039/d3ya00615h

rsc.li/energy-advances

The oxygen reduction reaction (ORR) kinetics are slow, limiting the overall reaction rate. It is still challenging to construct transition metal-based electrocatalysts with high activity and stability. In this study, FeN_x/Fe-based skewer-like N-doped carbon nanotubes (FeN_x/Fe-NCNTs) are successfully prepared by a simple one-step pyrolysis strategy. The Fe-based nanoparticles are evenly dispersed at the tip of the carbon nanotubes and the junction of the bamboo segments, indicating that the FeN_x/Fe-NCNTs catalyst has abundant ORR active sites. When applied to the ORR, FeN_x/Fe-NCNTs exhibit initial and half-wave potentials of 0.96 and 0.86 V (*vs.* RHE) in 0.1 M KOH, comparable to those of commercial 20% Pt/C catalysts. Moreover, the FeN_x/Fe-NCNTs showed a low Tafel slope value of 81.2 mV dec^{-1} and the electron transfer number (*n*) is between 3.81 and 3.93, indicating a fast four-electron transfer path. The results show that FeN_x/Fe-NCNTs have better electron transfer efficiency and stability, making them an excellent ORR catalyst.

Introduction

The demand for clean economic energy as an alternative to fossil fuels is currently growing in response to environmental concerns and energy consumption.[1–3] Fuel cells have been recognized as major alternative devices.[4,5] However, the sluggishness of the oxygen reduction reaction (ORR) in fuel cells is a major challenge. The high cost and lack of resources of highly active platinum (Pt)-based catalysts in the ORR have prevented their large-scale commercial application.[6–10] Transition metal and carbon-based materials have become the subject of lively discussion among researchers.[11–15]

As for carbon materials, how to improve the activity has also become a major focus of research. In recent years, nitrogen-doped carbon materials have shown excellent catalytic properties. The disparity in electronegativity between nitrogen and carbon atoms results in an imbalance in their electron spin density, and charge polarisation is an important reason for improving the catalytic performance of N-doped carbon materials. Additionally, the encapsulation of abundant transition metals (eg. Cu, Ni, Co, Fe) in N-doped carbon materials has positive implications for enhancing the electrocatalytic performance, because the abundant 3d electrons in transition metal elements are easily lost or captured, allowing for the controlled synthesis of multi-component, multi-structures as catalysts with multiple catalytic active centers, especially for Fe-based N-doped carbon materials.[16–19] However, developing transition metal oxygen reduction catalysts with high activity and excellent stability is still a problem in industry, since nanoparticles based on transition metals loaded on the outer surface of carbon materials are susceptible to Ostwald curing during the catalytic process, resulting in poor long-term stability.[20–24]

Prussian blue, a type of transition metal-based material, is widely utilized in synthesizing catalysts for electro-chemical power devices. Its widespread application results from its low cost, stable 3D framework, non-toxic and non-hazardous properties, and abundant natural resources.[25,26] Prussian blue can be used as a sacrificial template for conversion to inorganic nanoparticles and carbon composites can be created through a simple carbonization process, resulting in the uniform dispersion of metal or metal-based nanoparticles within the carbon matrix.[27]

In this regard, we explored a simple preparation method of Fe-based carbon nanotube materials for highly active ORR electrocatalysts with Fe-based nanoparticles as the main active site of the catalyst. $Na_4Fe(CN)_6$ and $FeCl_2{\cdot}4H_2O$ were homogeneously mixed, and a certain amount of HCl was added to prepare a Prussian blue precursor material, which was aged in

[a] *School of Material Science and Engineering, University of Jinan, Jinan 250022, Shandong, China*
[b] *State Key Lab of Electroanalytical Chemistry, Changchun Institute of Applied Chemistry, Chinese Academy of Sciences, Changchun 130022, Jilin, China. E-mail: mse_zhaozl@ujn.edu.cn*

† Electronic supplementary information (ESI) available. See DOI: https://doi.org/10.1039/d3ya00615h

‡ Zhenlu Zhao and Qidi Lu contributed equally to this work.

Open Access Article. Published on 12 februarie 2024. Downloaded on 01.06.2026 19:18:41.
This article is licensed under a Creative Commons Attribution-NonCommercial 3.0 Unported Licence.

© 2024 The Author(s). Published by the Royal Society of Chemistry

Open Access Article. Published on 12 februarie 2024. Downloaded on 01.06.2026 19:18:41.
This article is licensed under a Creative Commons Attribution-NonCommercial 3.0 Unported Licence.

air for 24 h. An appropriate amount of melamine was added and then homogeneously sintered in a tube furnace at 800 °C to form FeN_x/Fe-based N-doped carbon materials. The material (FeN_x/Fe-NCNTs) exhibits high ORR electrocatalytic activity in alkaline media, where the half-wave potential reaches 0.86 V and the onset potential is as high as 0.96 V (*vs.* RHE). The FeN_x/Fe-NCNTs show higher ORR activity with a peroxide yield of less than 8%, an electron transfer number close to 4, and improved stability compared to commercial 20% Pt/C.

Experimental

Preparation of Prussian blue

Synthesis of the Prussian blue ($Fe_4[Fe(CN)_6]_3$) precursor: 5 ml of an aqueous solution containing 300 mM $FeCl_2{\cdot}4H_2O$ and 600 mM $Na_4Fe(CN)_6$ was prepared, then 45 ml of concentrated hydrochloric acid (37%) was added, and the resultant solution was placed in a fume cupboard and aged for 24 h in air. The solution was centrifuged at 9000 rpm to obtain a precipitate and then it was washed three times with deionized water and ethanol. The samples were dried for 24 h at 70 °C.

Preparation of FeN_x/Fe-NCNTs

0.2 g of Prussian blue ($Fe_4[Fe(CN)_6]_3$) synthesized above was ground with 3 g of melamine and mixed well in a mortar and pestle, and then the ground sample was transferred to a porcelain boat. The porcelain boat was placed into a two-zone temperature-controlled tube furnace, and the sample was heated up to 800 °C under a N_2 atmosphere at a ramping rate of 3 °C min^{-1}. The FeN_x/Fe-NCNTs were obtained by holding at 800 °C for 2 h.

Results and discussion

As depicted in Fig. 1, FeN_x/Fe-NCNTs were prepared by adding hydrochloric acid to control the synthesis of synthetic Prussian blue precursors. The composition and structure of the FeN_x/Fe-NCNT catalyst were investigated by X-ray diffractometry (XRD). The XRD patterns (Fig. 2a) show crystal diffraction peaks of Prussian blue at 17.374° (100), 24.710° (110), 35.164° (200), 39.491° (210), 43.692° (211), 50.673° (220), 53.886° (300), 57.166° (310), 60.457° (311), 63.202° (222), 66.227° (320), 68.997° (321), 74.677° (400) and 76.807° (410). The diffraction peaks above correspond well with those of Prussian blue, which also proves the successful preparation of Prussian blue precursor. The XRD pattern of the FeN_x/Fe-NCNTs (Fig. 2b) shows that there are crystallization diffraction peaks at 26.381°, 43.915°, 44.673° and 65.021°. The diffraction peaks at 44.673° and 65.021° correspond to the (110) and (200) crystal planes of Fe. The 43.915° diffraction peak corresponds to the (111) crystal plane of FeN, and the 26.381° diffraction peak corresponds to the (002) crystal plane of C. Fig. 2c shows the N_2 adsorption–desorption curve of the FeN_x/Fe-NCNTs catalyst, which shows a typical Type IV isotherm indicating that the material has a large number of mesopores and has a clear hysteresis line. The FeN_x/Fe-NCNTs have a high surface area of 153.379 $m^2\ g^{-1}$. Fig. 2d displays the pore size distribution of the material, which is predominantly distributed within the 2–6 nm range. The high quantity of pores facilitates electron transfer, which improves the catalytic efficiency of the catalysts.[28]

Fig. 2e–h show the X-ray photoelectron spectroscopy (XPS) images of the samples to further analyze the material composition of the FeN_x/Fe-NCNTs. Fig. 2e shows the survey spectrum of the FeN_x/Fe-NCNTs. The survey spectrum indicates the presence of C, N, O and Fe. In the high-resolution XPS spectra of C 1s in Fig. 2f, the characteristic peaks at 284.8, 286.1 and 289.1 eV can be observed, belonging to C–C, C–N and O=C–O bonds, respectively.[29] Fig. 2g shows the high-resolution XPS spectrum of N 1s with peaks at 398.4 eV attributed to pyridine nitrogen, 399.3 eV to Fe–N, 401.0 eV to graphitic nitrogen, and 403.9 eV to nitrogen oxide.[30–32] The material's ORR activity benefits from the presence of pyridine nitrogen and graphitic nitrogen.[31] The high-resolution XPS spectrum of Fe 2p is shown in Fig. 2h. The peak at 706.7 eV belongs to zero-valent Fe $2p_{3/2}$, the peak at 709.9 eV belongs to Fe^{2+} $2p_{3/2}$, and the peak at 712.4 eV is Fe^{3+} $2p_{3/2}$.[30,31] In summary, the iron present in FeN_x/Fe-NCNTs is distributed throughout the N doped carbon matrix in the form of Fe, FeN, and Fe–N_x.[33]

Fig. 3a and b shows images obtained by field emission scanning electron microscopy (FESEM) of Prussian blue. The

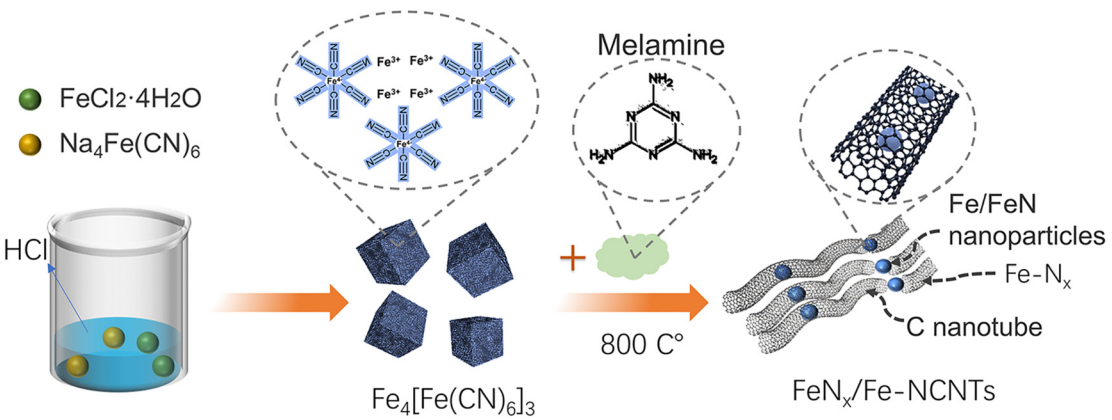

Fig. 1 Schematic diagram of the synthesis of FeN_x/Fe-NCNTs.

Open Access Article. Published on 12 februarie 2024. Downloaded on 01.06.2026 19:18:41.
This article is licensed under a Creative Commons Attribution-NonCommercial 3.0 Unported Licence.

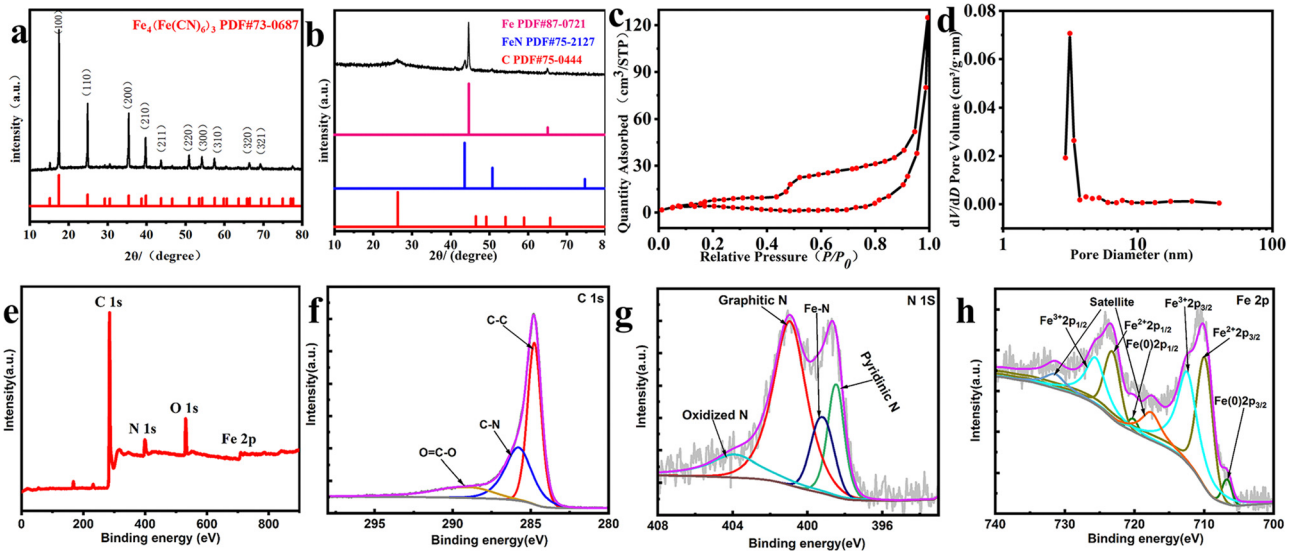

Fig. 2 XRD patterns of (a) Prussian blue and (b) FeN_x/Fe-NCNTs; (c) N_2 adsorption–desorption isotherm curve of the FeN_x/Fe-NCNTs; (d) pore size distribution curve of the FeN_x/Fe-NCNTs; XPS spectra of (e) survey, (f) C 1s, (g) N 1s, and (h) Fe 2p of FeN_x/Fe-NCNTs.

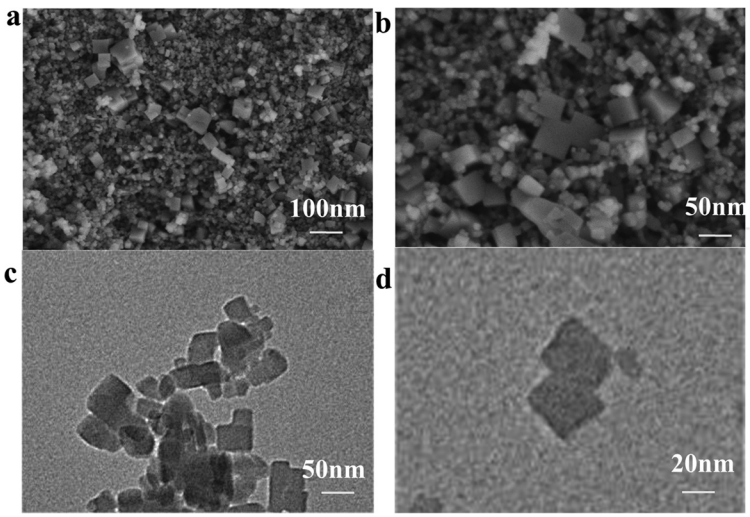

Fig. 3 (a) and (b) FESEM diagrams of Prussian blue; (c) and (d) TEM diagrams of Prussian blue.

images show that the size of the prepared cubes ranged from 20 to 100 nm. The results indicate the successful preparation of the cubes.[26] The transmission electron microscopy (TEM) images of Prussian blue in Fig. 3c and d further demonstrate the cubic structured Prussian blue material. The morphology and structure of the samples containing FeN_x/Fe-NCNTs were further characterized through the use of FESEM and TEM. As shown in the FESEM images of Fig. 4a and b, the FeN_x/Fe-NCNT samples have narrow and dense carbon nanotube structures, which have an average diameter of about 500 nm, with uniform thickness and length. The TEM images of Fig. 4c and d show the presence of Fe-based nanoparticles, especially at the tips and bamboo-like junctions of the FeN_x/Fe-NCNTs. These nanoparticles significantly increase the material's surface area, number of defects, and electrical conductivity while simultaneously supporting an increase in active sites. The overall effect is an improvement in the ORR performance of the material.[34] Fig. 4e–h displays the energy dispersive X-ray spectral (EDS) mapping of the material, revealing that the Fe-based nanoparticles are predominantly concentrated at the carbon nanotube tips while also existing within the interior and on the surface of the carbon nanotubes. Nitrogen is found to be uniformly distributed throughout the structure, indicating that pyrolysis can uniformly dope a large amount of N heteroatoms into the carbon material.[35] EDS further confirms that the iron within FeN_x/Fe-NCNTs is distributed throughout the N-doped carbon matrix as Fe, FeN, and Fe–N_x.

The electrochemical ORR properties of FeN_x/Fe-NCNTs are next investigated, and the electrocatalytic activity of the FeN_x/Fe-NCNTs is tested by cyclic voltammetry (CV). As shown in Fig. 5a, there is a clear redox peak in the O_2-saturated 0.1 M KOH solution compared to the N_2-saturated 0.1 M KOH

© 2024 The Author(s). Published by the Royal Society of Chemistry

Open Access Article. Published on 12 februarie 2024. Downloaded on 01.06.2026 19:18:41.
This article is licensed under a Creative Commons Attribution-NonCommercial 3.0 Unported Licence.

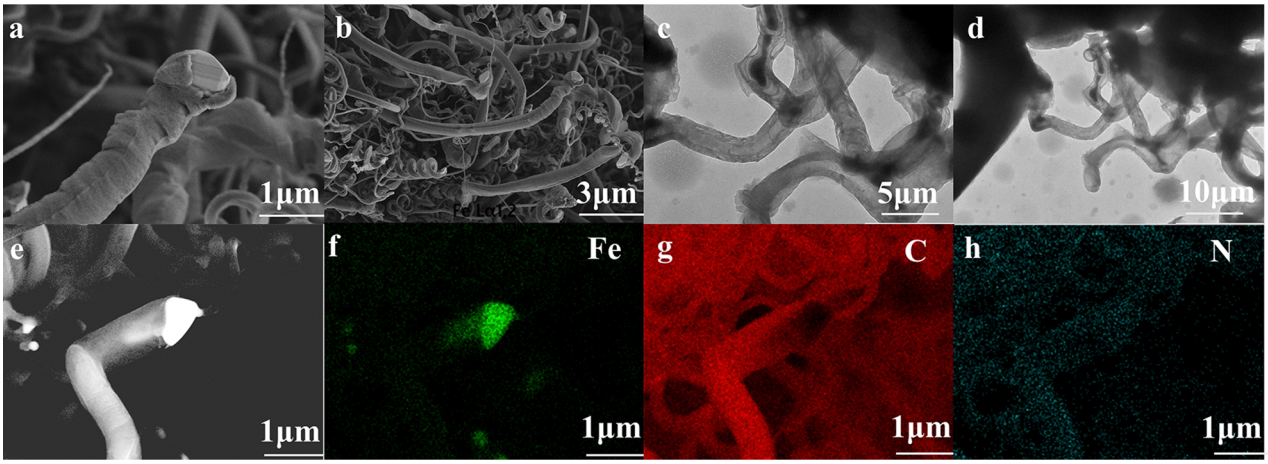

Fig. 4 (a) and (b) FESEM images of FeN_x/Fe-NCNTs; (c) and (d) TEM images of FeN_x/Fe-NCNTs; (e) EDS surface scan composition distribution of FeN_x/Fe-NCNTs: (f) Fe; (g) C; (h) N.

solution, and there is a peak at about 0.61 V. Furthermore, a peak at approximately 0.61 V indicates the exceptional ORR activity of the catalyst. Linear scanning voltammetry (LSV) curves measured at different velocities further show that FeN_x/Fe-NCNTs have a high ORR activity (Fig. 5b) with an onset potential of 0.96 V and a half-wave potential ($E_{1/2}$) of 0.86 V (*vs.* RHE), which are almost comparable to that of the commercial 20% Pt/C (0.87 V), or even have a better onset potential (Fig. 5d). The K–L curve, as computed from the LSV (Fig. 5c), yields 3.81–3.93 for the electron transfer number (n) within the potential range of 0.3 to 0.7 V. This indicates that the material's ORR in the limit current region involves nearly 4 transferred electrons. The ORR activity of the FeN_x/Fe-NCNTs and other reported transition metal-based carbon electrocatalysts were compared (Table S1, ESI†). The FeN_x/Fe-NCNTs exhibit excellent ORR activity. The ORR activity of the FeN_x/Fe-NCNTs is improved by the synergistic enhancement effect of the N-doped carbon nanotubes and FeN_x/Fe-based nanoparticles, which facilitates mass and electron transport and improves the activity of the active sites.

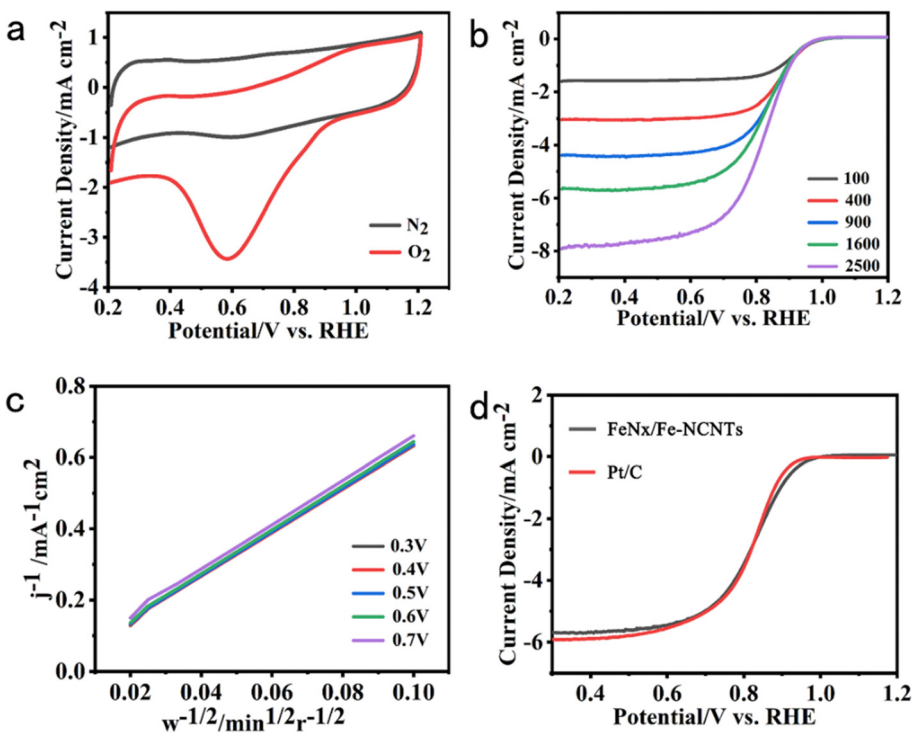

Fig. 5 Electrochemical ORR experiments of FeN_x/Fe-NCNTs and Pt/C: (a) CV curves (the black and red lines recorded at a sweeping speed of 50 mV s^{-1} in a 0.1 M KOH solution saturated with N_2 and O_2, correspondingly); (b) LSV curves of FeN_x/Fe-NCNTs at different sweep rates; (c) K–L plots of FeN_x/Fe-NCNTs (ω is the rotational speed); (d) LSV curves of Pt/C and FeN_x/Fe-NCNTs (1600 rpm).

© 2024 The Author(s). Published by the Royal Society of Chemistry

Open Access Article. Published on 12 februarie 2024. Downloaded on 01.06.2026 19:18:41.
This article is licensed under a Creative Commons Attribution-NonCommercial 3.0 Unported Licence.

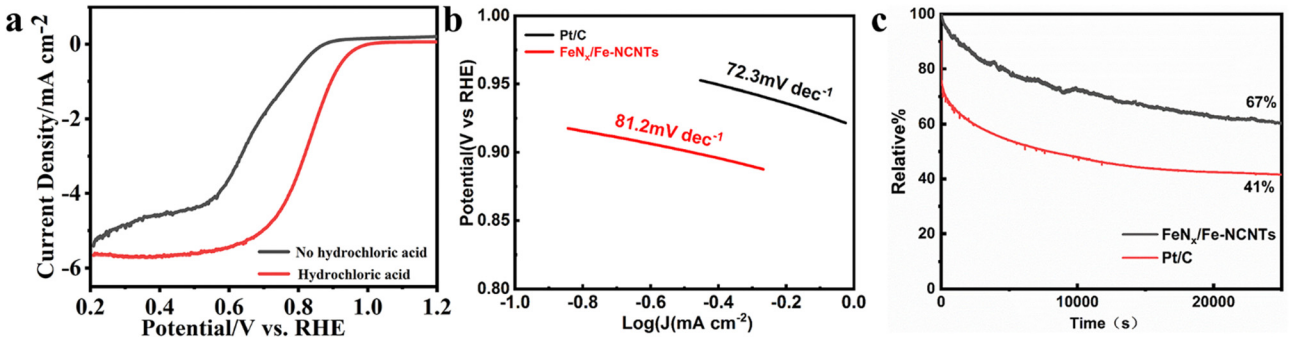

Fig. 6 (a) LSV curves of FeN_x/Fe-NCNTs in the presence or absence of hydrochloric acid (1600 rpm); (b) Tafel slopes of FeN_x/Fe-NCNTs and Pt/C catalysts; (c) chronoamperometry of FeN_x/Fe-NCNTs and Pt/C at 0.6 V (*vs.* RHE).

From Fig. 6a, it can be seen that the FeN_x/Fe-NCNTs catalyst with 45 ml of concentrated hydrochloric acid has a better ORR activity with an onset potential of 0.96 V and a half-wave potential ($E_{1/2}$) of 0.86 V (*vs.* RHE). The sample without hydrochloric acid treatment has a worse ORR activity with an onset potential of only 0.85 V and a half-wave potential of only 0.67 V (*vs.* RHE). Concentrated hydrochloric acid plays a vital role in enhancing the catalyst activity under similar pyrolysis conditions. This effect may relate to the synthesis of the Prussian blue precursor. In the preparation of this experiment, 45 ml of concentrated hydrochloric acid (37% HCl) was added as an inhibitor for the synthesis of Prussian blue. The initial Gibbs free energy difference (ΔG) between the reactants and products of the synthesized Prussian blue is less than zero and the reaction reacts spontaneously. Protons can react with $[Fe(CN)_6]^{4-}$ to form $H_4[Fe(CN)_6]$, which makes the Gibbs free energy of the synthesis of Prussian blue reaction decrease and the trend and rate of the reaction decrease. Volatile hydrochloric acid was used as a source of protons, and with the volatilization of the hydrochloric acid, the concentration of protons in the reaction system decreased, and the synthetic Prussian blue reaction proceeded gradually and spontaneously to form small-sized Prussian blue. The reaction system cannot be hermetically sealed. If it is hermetically sealed, then the internal inhibitor concentration will become so great that the reaction to synthesize Prussian blue will not be able to continue spontaneously.[36] The Tafel slope curve of our prepared FeN_x/Fe-NCNTs is shown in Fig. 6b above, from which it can be seen that the Tafel slope value of FeN_x/Fe-NCNTs is 81.2 mV dec^{-1}, which is close to that of the commercial 20% Pt/C catalyst (72.3 mV dec^{-1}). The results show that the FeN_x/Fe-NCNTs catalysts have superior electron transfer efficiency and chemical reaction kinetics. Fig. 6c shows the chronoamperometry of FeN_x/Fe-NCNTs at 0.6 V (*vs.* RHE). It maintains 66.7% performance after 25 000 s of chronoamperometry, while commercial 20% Pt/C has higher current loss and only maintains about 53.6% performance, indicating that our synthesized FeN_x/Fe-NCNTs have better long-term stability, which makes them an excellent electrochemical catalyst for the ORR.

Conclusion

In summary, a bamboo nanotube-like structural material with uniform diameter was successfully prepared by a simple one-step pyrolysis strategy, and Fe-based nanoparticles were homogeneously dispersed at the tips of the carbon nanotubes and the junctions of the bamboo joints. The FeN_x/Fe-NCNTs catalysts are rich in active sites. The ORR test of the FeN_x/Fe-NCNTs material shows that the onset potential and half-wave potential in 0.1 M KOH are 0.96 and 0.86 V (*vs.* RHE), respectively, which are almost comparable to the commercial 20% Pt/C catalysts with even more excellent onset potential. This indicates that our prepared materials have excellent ORR electrocatalytic activity. In addition, FeN_x/Fe-NCNTs have better stability, which makes them an excellent ORR electrochemical catalyst. The FeN_x/Fe-NCNTs were prepared in a simple method with convenient operation steps and possessed excellent ORR electrocatalytic activity.

Author contributions

Zhenlu Zhao conceived and designed the project. Qidi Lu prepared the nanomaterials, conducted the structural characterizations, and performed electrical measurements. Zhenlu Zhao, Qidi Lu and Xin Wang analyzed and discussed the data. Zhenlu Zhao and Qidi Lu wrote the manuscript. All authors have given approval to the final version of the paper.

Conflicts of interest

There are no conflicts to declare.

Acknowledgements

We acknowledge the financial support from the Natural Science Foundation of Shandong Province (No. ZR2021MB017), Foundation of State Key Laboratory of Electro-analytical Chemistry (SKLEAC201907), and Study Abroad Fund.

References

1 B. You and Y. Sun, *Acc. Chem. Res.*, 2018, **51**, 1571–1580.
2 Z. Dimitrova and W. B. Nader, *Energy*, 2022, **239**, 121933–121944.

© 2024 The Author(s). Published by the Royal Society of Chemistry

Open Access Article. Published on 12 februarie 2024. Downloaded on 01.06.2026 19:18:41.
This article is licensed under a Creative Commons Attribution-NonCommercial 3.0 Unported Licence.

3 V. Mazumder, M. Chi, K. L. More and S. Sun, *J. Am. Chem. Soc.*, 2010, **132**, 7848–7849.
4 L. Wu, Q. Li, C. H. Wu, H. Zhu, A. Mendoza-Garcia, B. Shen, J. Guo and S. Sun, *J. Am. Chem. Soc.*, 2015, **137**, 7071–7074.
5 H. Liu, Y. Zheng, G. Wang and S. Z. Qiao, *Adv. Energy Mater.*, 2015, **5**, 1401186–1401192.
6 S.-Y. Lin, Y.-P. Chen, Y. Cao, L. Zhang, J.-J. Feng and A.-J. Wang, *J. Power Sources*, 2022, **521**, 230926–230934.
7 Y. Feng, K. Song, W. Zhang, X. Zhou, S. J. Yoo, J.-G. Kim, S. Qiao, Y. Qi, X. Zou, Z. Chen, T. Qin, N. Yue, Z. Wang, D. Li and W. Zheng, *J. Energy Chem.*, 2022, **70**, 211–218.
8 X. Liu, L. Wang, P. Yu, C. Tian, F. Sun, J. Ma, W. Li and H. Fu, *Angew. Chem., Int. Ed.*, 2018, **57**, 16166–16170.
9 X. Wang, H. Zhu, C. Yang, J. Lu, L. Zheng and H.-P. Liang, *Carbon*, 2022, **191**, 393–402.
10 H. Karimi-Maleh, C. Karaman, O. Karaman, F. Karimi, Y. Vasseghian, L. Fu, M. Baghayeri, J. Rouhi, P. Senthil Kumar, P.-L. Show, S. Rajendran, A. L. Sanati and A. Mirabi, *J. Nanostruct. Chem.*, 2022, **12**, 429–439.
11 J. Liang, Y. Zheng, J. Chen, J. Liu, D. Hulicova-Jurcakova, M. Jaroniec and S. Z. Qiao, *Angew. Chem., Int. Ed.*, 2012, **51**, 3892–3896.
12 S. Sarkar, N. Kamboj, M. Das, T. Purkait, A. Biswas and R. S. Dey, *Inorg. Chem.*, 2020, **59**, 1332–1339.
13 H.-S. Zhai, L. Cao and X.-H. Xia, *Chin. Chem. Lett.*, 2013, **24**, 103–106.
14 J. Hu, P. Zhang, W. An, L. Liu, Y. Liang and W. Cui, *Appl. Catal., B*, 2019, **245**, 130–142.
15 Q. Liu, T. Chen, Y. Guo, Z. Zhang and X. Fang, *Appl. Catal., B*, 2017, **205**, 173–181.
16 S. Sarkar, S. S. Sumukh, K. Roy, N. Kamboj, T. Purkait, M. Das and R. S. Dey, *J. Colloid Interface Sci.*, 2020, **558**, 182–189.
17 R. Li, J. Huang, M. Cai, J. Huang, Z. Xie, Q. Zhang, Y. Liu, H. Liu, W. Lv and G. Liu, *J. Hazard. Mater.*, 2020, **384**, 121435–121445.
18 P. Teppor, R. Jäger, E. Härk, I. Tallo, U. Joost, M. Kook, P. Paiste, K. Šmits, K. Kirsimäe and E. Lust, *J. Electrochem. Soc.*, 2018, **165**, F1217–F1223.
19 O. Pariiska, D. Mazur, Y. Kurys, R. Socha, V. Koshechko and V. Pokhodenko, *J. Solid State Electrochem.*, 2021, **25**, 2309–2319.
20 J. Zhang, S. Guo, J. Wei, Q. Xu, W. Yan, J. Fu, S. Wang, M. Cao and Z. Chen, *Chem. – Eur. J.*, 2013, **19**, 16087–16092.
21 D. Deng, L. Yu, X. Chen, G. Wang, L. Jin, X. Pan, J. Deng, G. Sun and X. Bao, *Angew. Chem., Int. Ed.*, 2013, **52**, 371–375.
22 Q. Li, H. Pan, D. Higgins, R. Cao, G. Zhang, H. Lv, K. Wu, J. Cho and G. Wu, *Small*, 2015, **11**, 1443–1452.
23 Y.-G. Guo, J.-S. Hu and L.-J. Wan, *Adv. Mater.*, 2008, **20**, 2878–2887.
24 Y. Ren, R. Chang, X. Hu, J. Guo, G. Hao and A. Lu, *Chin. Chem. Lett.*, 2023, **34**, 108634.
25 S. Cheng, C. Shen, H. Zheng, F. Liu and A. Li, *Appl. Catal., B*, 2020, **269**, 118785–118794.
26 J. Sanetuntikul and S. Shanmugam, *Electrochim. Acta*, 2014, **119**, 92–98.
27 J. Huai, K. Ma, Y. Lu, T. Chen and Z. Zhao, *ChemCatChem*, 2019, **11**, 4818–4821.
28 X. Xie, L. Peng, H. Yang, G. I. N. Waterhouse, L. Shang and T. Zhang, *Adv. Mater.*, 2021, **33**, 2101038–2101045.
29 H. Niu, Y. Zhang, Y. Liu, B. Luo, N. Xin and W. Shi, *J. Mater. Chem. A*, 2019, **7**, 8503–8509.
30 X. Wan, Q. Liu, J. Liu, S. Liu, X. Liu, L. Zheng, J. Shang, R. Yu and J. Shui, *Nat. Commun.*, 2022, **13**, 2963–2973.
31 F. Fan, H. Zhou, R. Yan, C. Yang, H. Zhu, Y. Gao, L. Ma, S. Cao, C. Cheng and Y. Wang, *ACS Appl. Mater. Interfaces*, 2021, **13**, 41609–41618.
32 S.-Y. Tang, Y.-S. Wang, Y.-F. Yuan, Y.-Q. Ba, L.-Q. Wang, G.-P. Hao and A.-H. Lu, *New Carbon Mater.*, 2022, **37**, 237–244.
33 J. Han, H. Bao, J.-Q. Wang, L. Zheng, S. Sun, Z. L. Wang and C. Sun, *Appl. Catal., B*, 2021, **280**, 119411–119420.
34 X. Liu, W. Yang, L. Chen, Z. Liu, L. Long, S. Wang, C. Liu, S. Dong and J. Jia, *ACS Appl. Mater. Interfaces*, 2020, **12**, 4463–4472.
35 Z. Zhao, C. Gao, K. Ma and Y. Lu, *Appl. Surf. Sci.*, 2020, **504**, 144380–144385.
36 W. Zhang, Y. Li, C. Shi, R. Qi and M. Hu, *J. Am. Chem. Soc.*, 2021, **143**, 6447–6459.

© 2024 The Author(s). Published by the Royal Society of Chemistry